Available online at www.sciencedirect.com
ScienceDirect
Trans. Nonferrous Met. Soc. China 33(2023) 789−801
Transactions of Nonferrous Metals Society of China
www.tnmsc.cn

Interfacial-constraint-induced intragranular deformation inhomogeneity of Ti−Al layered composites

Xin-bo NI[1], Zhuang-zhuang LIU[1], Ke-song MIAO[2,3], Jin-feng LENG[1], Guo-hua FAN[2], Xin-ying TENG[1], Hao WU[2]

1. School of Materials Science and Engineering, University of Jinan, Jinan 250022, China;
2. Key Laboratory for Light-weight Materials, Nanjing Tech University, Nanjing 211816, China;
3. School of Materials Science and Engineering, Harbin Institute of Technology, Harbin 150001, China

Received 30 September 2021; accepted 22 February 2022

Abstract: A multilayered Ti−Al composite was designed and fabricated by hot pressing and hot rolling of alternately stacked Ti and Al foils. In situ electron backscatter diffraction was utilized to characterize the orientation evolution and deformed substructure upon tension. A remarkably inhomogeneous deformation mode was observed within the interior of Ti grains, in a way that the closer to the grain boundary or Ti/Al interfaces, the harder the plastic flow. Such a phenomenon is attributed to the synergetic constraint of phase interface and grain boundary. The present study thus provides a new strategy to tailor the deformation behavior of metallic materials by sufficiently leveraging the interfacial constraint effect for performance optimization.

Key words: layered composites; plastic deformation; electron backscatter diffraction; interfacial constraint

1 Introduction

Titanium and its alloys have been widely used for industrial and aerospace applications owing to their high specific strength and corrosion resistance [1−3]. Nevertheless, α-Ti usually exhibits poor plasticity due to insufficient slip systems associated with the hexagonal close-packed (hcp) structure [4,5]. It is well known that prismatic $\langle a \rangle$ slip is the easiest slip system to be activated, whereas the activation of pyramidal $\langle c+a \rangle$ slip and twinning are much more difficult owing to the significant difference in critical resolved shear stress [6−8]. To reconcile the anisotropic deformation mode, novel microstructures and related plasticity mechanisms were proposed. As an example, unique three-dimensionally heterogeneous harmonic Ti, characterized by a controlled bimodal grain size distribution, was produced through a powder metallurgy processing approach [9]. Such an inhomogeneous microstructure accommodated the stress concentration efficiently and stabilized the plastic flow [10−12]. Therefore, the work hardening capacity of harmonic Ti was remarkably enhanced, endowing hcp Ti with ductility [13−16].

In addition to the harmonic structure, layered composites have also attracted much attentions because of their sharp interface as well as the interfacial constraint effect [17]. A successful attempt was made on Ti−Al layered metals, fabricated by hot-rolling and annealing of pure Ti and Al sheets [18]. The strong interfacial constraint promoted the strain transferring from Ti layers to adjacent Al layers, which thus relieved the degree of strain localization and helped with enhancing the tensile ductility of hcp Ti. WU and co-workers [19] proposed a thermomechanical route of asymmetric rolling and subsequent partial recrystallization to produce a new heterogeneously lamellar Ti.

Corresponding author: Xin-ying TENG, E-mail: mse_tengxy@ujn.edu.cn; Hao WU, E-mail: hwu@njtech.edu.cn
DOI: 10.1016/S1003-6326(23)66146-1

Experiments indicated a good combination of the strength of ultrafine-grain and the ductility of coarse-grain, because of the contribution of interfaces in impeding the dislocation motion and facilitating the dislocation pile-up and interaction. LI et al [20] prepared TiAl/Ti_2AlNb layered composites by vacuum hot pressing and demonstrated that the prominent tensile property was associated with the superior co-deformation ability of both constituent layers. More importantly, the application of heterogeneous layered strategy may induce the strain partitioning and change the stress state from uniaxial stress to multi-axial stress [10−14,16]. Note that the latter is beneficial to activating more slip or twinning systems so as to assist the plastic deformation [21]. Our recent work also demonstrated that under the effect of interfacial constraints, a large number of $\langle c+a \rangle$ dislocations were counterintuitively initiated after yielding, thereby causing significant strengthening [22]. However, the grain-level localized flow behavior and deformation heterogeneity, as well as their physical mechanism, remain unclear.

In the present study, we designed and fabricated a multilayered composite consisting of alternately stacked Ti and Al layers. The plastic deformation and grain rotation of hcp Ti were characterized by in situ electron backscatter diffraction (EBSD). The influence of interfacial constraints on the intragranular deformation heterogeneity was particularly discussed and elucidated.

2 Experimental

Commercially pure Ti and pure Al were cut into 150 mm × 150 mm sheets. The sample manufacturing procedure included surface pre-treatment, hot pressing, multi-pass rolling, and annealing. Firstly, the Ti sheets and Al sheets were thinned down to 200 μm using 10 vol.% HF solution and 10 wt.% NaOH solution, respectively, followed by ultrasonic cleaning with ethanol and drying. After surface pretreatment, alternately stacked Ti sheets and Al sheets with outside Ti sheets were placed into a graphite mold for vacuum hot pressing at 500 °C under 20 MPa for 1 h. Thirdly, the hot-pressed sample was subsequently multipass hot-rolled with a total thickness reduction of ~25% after 5 rolling passes and annealed at 500 °C for 10 min after each rolling pass. Finally, the hot-rolled sample was annealed at 500 °C for 1 h.

The microstructure of the as-prepared Ti−Al layered composites was examined by a TESCAN S8000GMH scanning electron microscope (SEM) equipped with an EDAX EBSD facility. The sample was mechanically ground and electrochemically polished using a solution composed of 60% methanol, 35% butyl glycol, and 5% perchloric acid at a temperature of −20 °C. In situ EBSD data were collected with a step size of 0.8 μm, a working distance of 15 mm, an accelerating voltage of 20 kV, and a current of 20 nA. All EBSD data were post-processed by OIM and MTEX software. Slip trace analysis was performed at the backscattering mode of SEM with a current of 3 nA, an accelerating voltage of 20 kV, and a working distance of 10 mm.

In situ EBSD characterization of Ti−Al layered composites was performed using a Mini-MTS tensile stage which was installed into a TESCAN S8000GMH SEM chamber. The sample size was 25 mm in length, 1.5 mm in width, and 2 mm in thickness. Such a tensile sample was machined by electrical discharge and deformed at a displacement rate of 12.5 μm/s. The working parameters for EBSD mapping were the same as those mentioned above.

3 Results and discussion

3.1 Microstructure

Figure 1 shows the microstructure of the as-prepared Ti−Al layered composites, featuring periodically stacked Ti and Al layers. They were both 150 μm in thickness; in between them, the layer interface was relatively straight and uninterrupted. No cracks and visible interfacial reactions were detected at the interface (Fig. 1(a)). We further characterized the microstructure by EBSD. Our results indicated a bimodal grain size distribution, composed of alternating coarse-grained Al and fine-grained Ti, as shown in the inverse pole figure (IPF, Fig. 1(b)). The average grain size of Ti layers was 35 μm (Fig. 1(c)), which possessed a typical basal texture with a bimodal distribution along the transverse direction (TD), as shown in Fig. 1(d).

3.2 Intragranular deformation inhomogeneity

Figure 2 shows the orientation evolution of Ti layers during in situ tension. The loading direction is parallel to TD. The black area in Fig. 2 represented the Kikuchi diffraction pattern that was not indexed owing to the deformation-induced

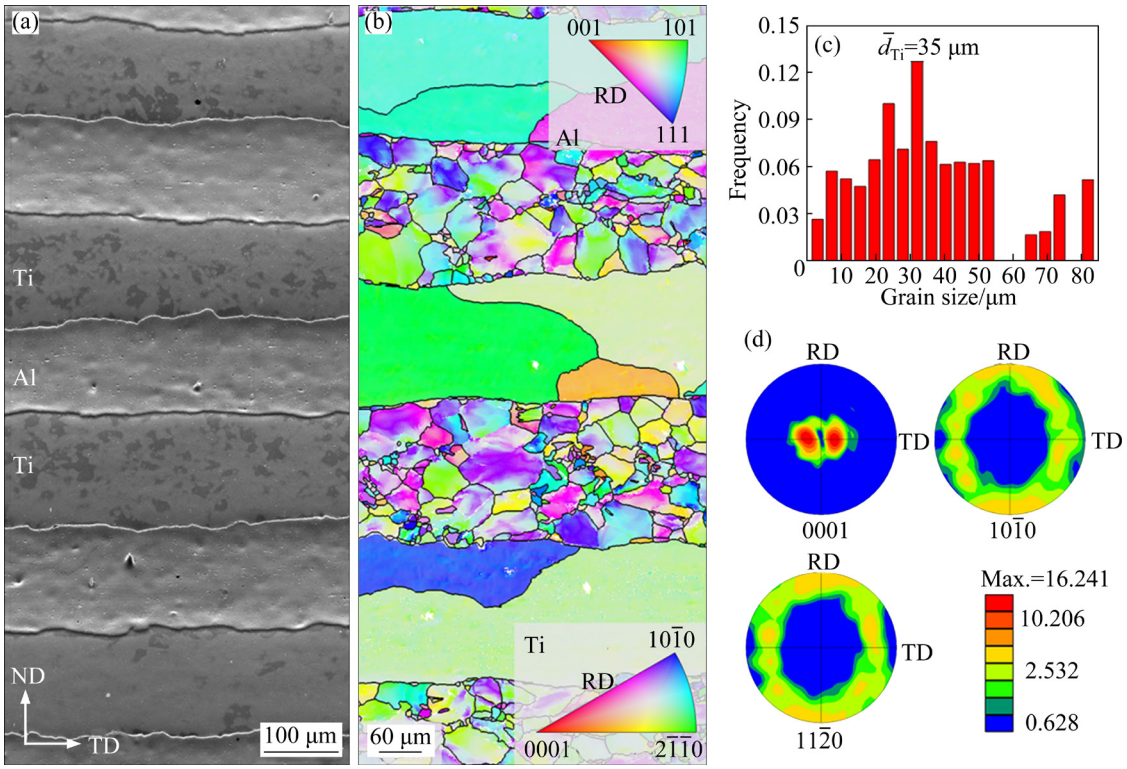

Fig. 1 Microstructure characterization: (a, b) SEM and EBSD mapping of as-prepared Ti−Al layered composites; (c) Distribution of grain size in Ti layers; (d) Texture analysis via pole figures (RD: Rolling direction; ND: Normal direction; TD: Transverse direction)

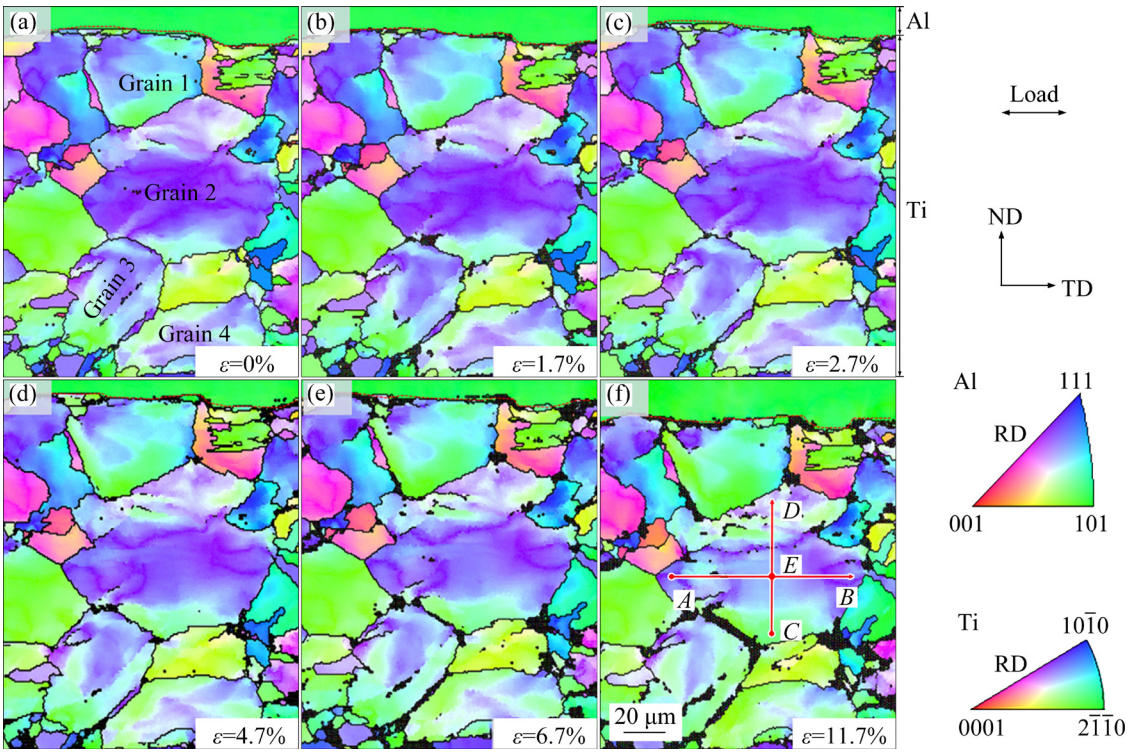

Fig. 2 In situ EBSD mappings during tensile deformation of Ti−Al layered composites at different strains: (a) 0%; (b) 1.7%; (c) 2.7%; (d) 4.7%; (e) 6.7%; (f) 11.7%

surface roughness. The phase interface was indicated by the red line, on top of which is Al and below which is the Ti layer. Grains 1−4 were selected as the grains of interest, which covered almost the entire Ti layer along ND. It was clearly observed that the orientation of the middle part in these grains seemed to be changed to a greater extent, while that of the part approaching to the grain boundary was varied slightly (Fig. 2). Grain 2 was thus selected as the main research object in the present study. Figure 3 illustrates the intragranular misorientation of Grain 2 along TD (Point *A* to *B*) and ND (Point *C* to *D*) at different strains. As the strain increased, the misorientation was gradually elevated along TD, as opposed to the neglected orientation variation along ND upon deformation (Fig. 3(b)).

Figure 4 shows the IPF and pole figures of Grain 2 at different tensile strains. The region of interest (ROI) was highlighted by the red rectangle.

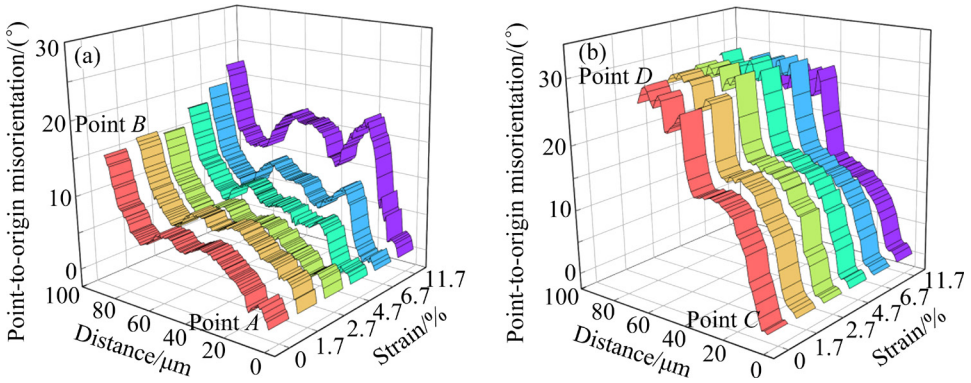

Fig. 3 Point-to-origin misorientation within Grain 2 at different tensile strains: (a) From Point *A* to Point *B* along TD; (b) From Point *C* to Point *D* along ND (Points *A*−*D* are highlighted in Fig. 2(f))

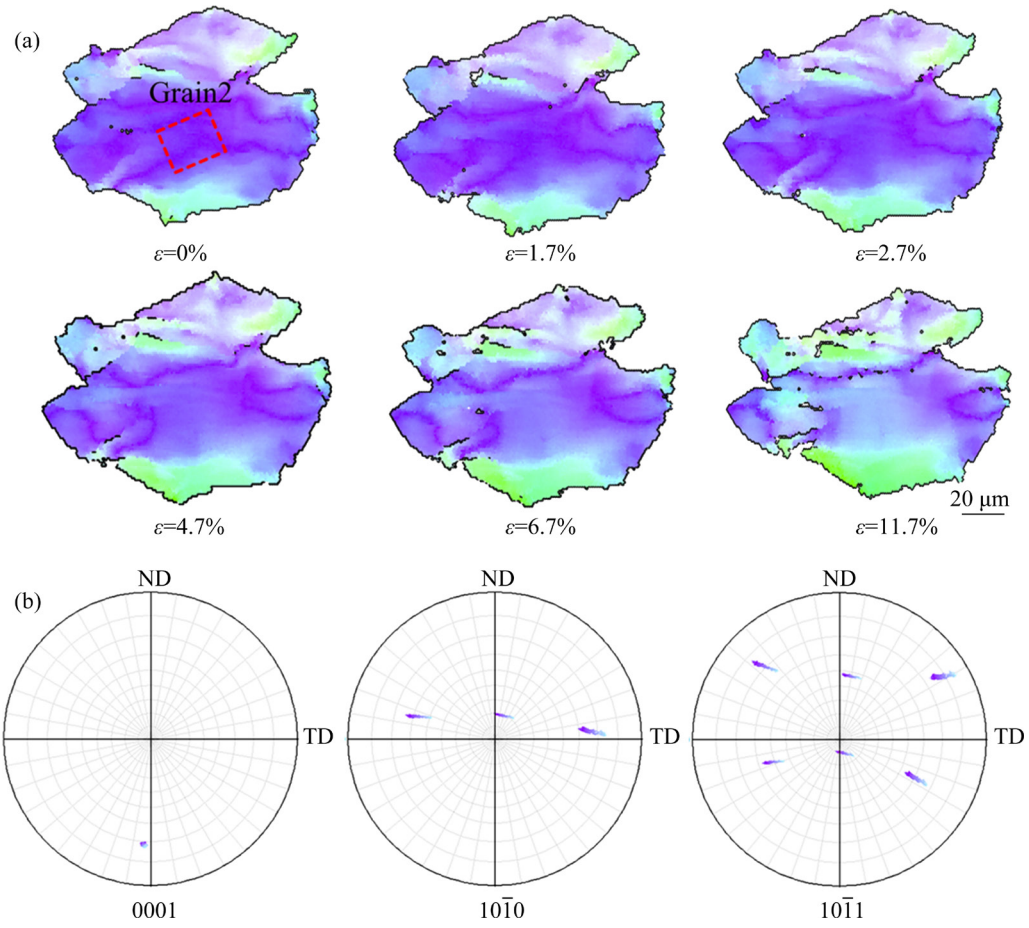

Fig. 4 Strain-induced intragranular rotation: (a) IPF mapping of Grain 2; (b) {0001}, {10$\bar{1}$0} and {10$\bar{1}$1} pole figures at region of interest as plotted by red rectangle in (a)

All the pole figures were composed of a group of concentric circles and the difference between two adjacent concentric circles was 10°. For the {0001} pole figure, the spots were not elongated, implying that the {0001} at the ROI was not rotated under tension. By contrast, the $\{10\bar{1}0\}$ and $\{10\bar{1}1\}$ for the ROI of the grain have rotated by an angle of about 12°. In order to quantify the intragranular rotation, Euler angles at different points in Grain 2 were extracted from EBSD data. According to Tables 1 and 2, the interior of Grain 2, as indicated by Point *E* in Fig. 2(f), was presented as a rotation angle of 5.8°, if a strain of 4.7% was applied, almost doubling that at the region near the grain boundary (Points *A*−*D*). A similar trend was re-appeared when the tensile strain was elevated from 4.7% to 11.7%.

We further quantified the Taylor axis of crystal rotation using the method of in-grain misorientation axes (IGMA). Such an EBSD-based analytical technology has been proven to be effective in elucidating the deformation mechanism of poly-crystalline hcp metals [23]. The IGMA mapping was obtained by (1) extracting the orientation information of the grain of interest, (2) determining the misorientation axes for all possible neighboring scanning-grid-point pairs, and (3) contouring the density of the misorientation axes onto the standard unit triangle with units of multiple uniform distribution (mud). Our results (Fig. 5) revealed that the range of misorientation was 1.2°−2° and verified that the activated slip system at the ROI was

Table 1 Intragranular rotation angle (ϕ_1, ϕ, ϕ_2) and axis analysis results at different tensile strains along TD

ε/%	Point *A*	Point *E*	Point *B*
0	(79°, 109°, 357°)	(265°, 71°, 181°)	(91°, 108°, 296°)
	⇩2.5° [$\bar{7}$13]	⇩5.8° [126]	⇩2.8° [$\bar{2}\bar{3}$0]
4.7	(77°, 108°, 355°)	(266°, 71°, 55°)	(89°, 110°, 295°)
	⇩3.6° [021]	⇩6.1° [0$\bar{1}$4]	⇩1.6° [$\bar{3}\bar{2}\bar{3}$]
11.7	(254°, 71°, 68°)	(266°, 72°, 169°)	(270°, 70°, 66°)

Table 2 Intragranular rotation angle (ϕ_1, ϕ, ϕ_2) and axis analysis results at different tensile strains along ND

ε/%	Point *C*	Point *E*	Point *D*
0	(266°, 62°, 68°)	(265°, 71°, 181°)	(266°, 73°, 44°)
	⇩2.8° [$\bar{2}\bar{1}\bar{2}$]	⇩5.8° [126]	⇩2.6° [32$\bar{1}$]
4.7	(267°, 63°, 190°)	(266°, 71°, 55°)	(85°, 105°, 318°)
	⇩2.6° [1$\bar{2}$5]	⇩6.1° [0$\bar{1}$4]	⇩2.8° [$\bar{1}\bar{8}\bar{4}$]
11.7	(268°, 63°, 72°)	(266°, 72°, 169°)	(86°, 107°, 260°)

prismatic ⟨*a*⟩ slip, echoing to the strong basal texture of ⟨0001⟩//ND [24]. The IGMA finding also agrees well with the IPF evolution that the $\langle 10\bar{1}0\rangle$ axis was gradually re-orientated toward the TD with increasing strains (Fig. 5(a)).

Figure 6 shows the Schmid factor of five different slip systems of Grain 2. It is observed that the average Schmid factor of prismatic ⟨*a*⟩ slip was the greatest, as opposed to the minimum value of basal slip. Hence, the prismatic ⟨*a*⟩ slip was considered as the preferred deformation mode. In

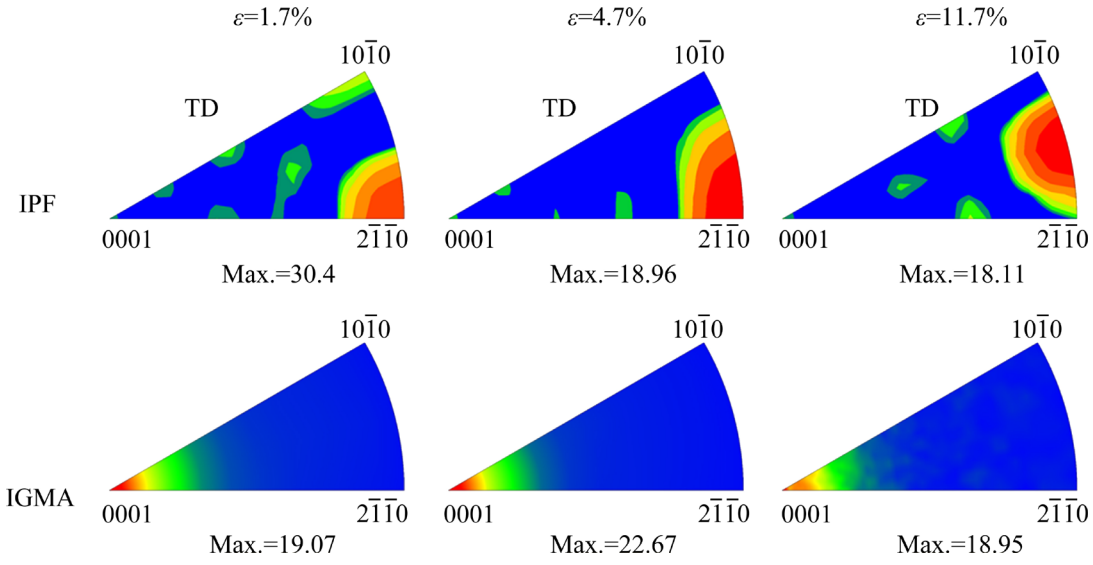

Fig. 5 Evolution of IPF and IGMA distribution with increasing tensile strains (The ROI is plotted by red rectangle in Fig. 4(a))

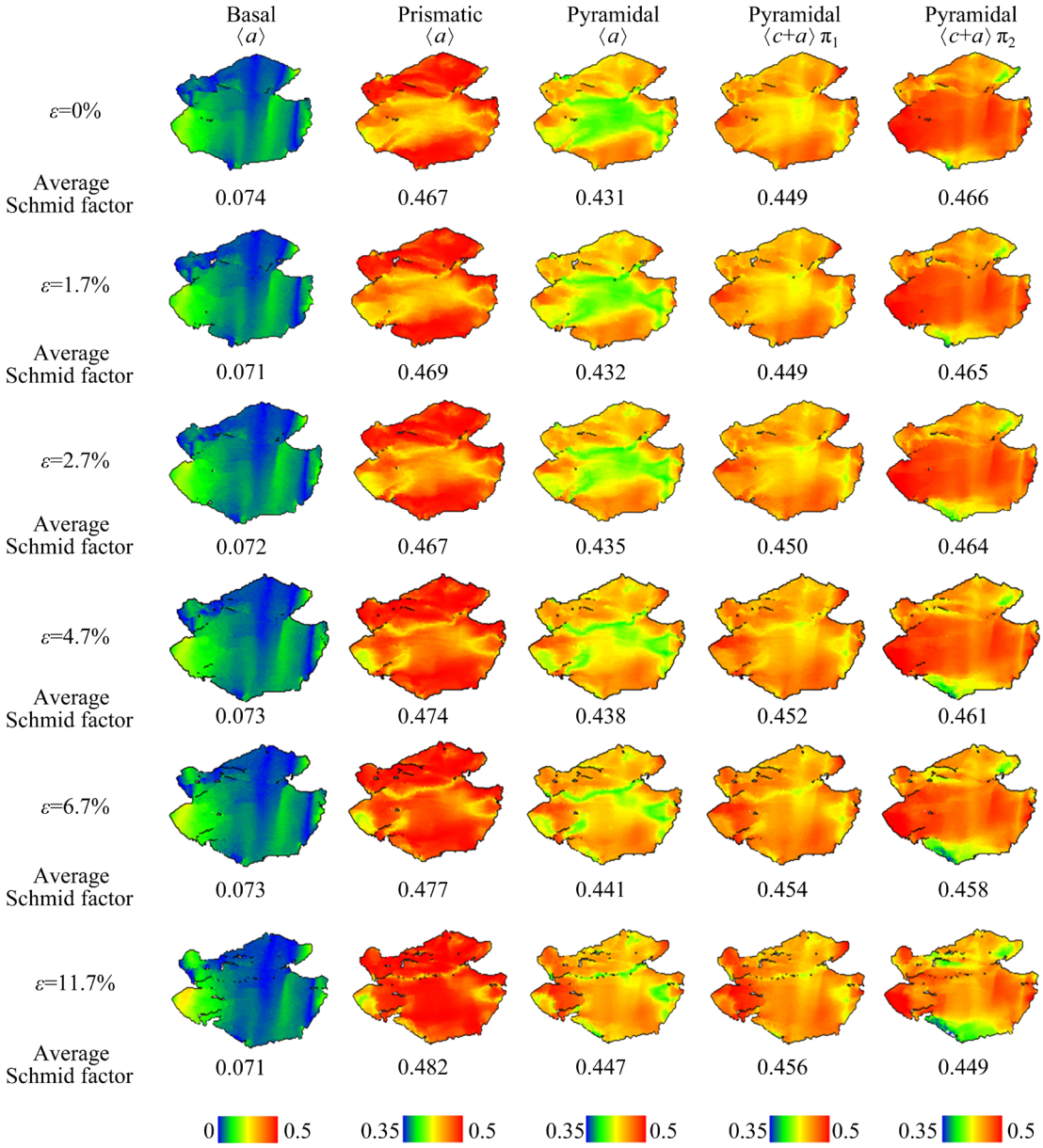

Fig. 6 Evolution of Schmid factors of basal, prismatic, and pyramidal slip for Grain 2 under tension

addition, the blue and the red slip trace in Fig. 7 also indicated that the operative slip system at the ROI was prismatic ⟨*a*⟩ slip. Such a prediction through the calculation of the Schmid factor also coincides well with experiment results by IGMA (Fig. 5). The cross-slip (pink and green lines) was frequently detected, and the activated slip system was identified as prismatic ⟨*a*⟩ slip.

Figure 8 indicates the distribution and evolution of grain boundaries during tension. Two main types of boundaries were visible: high-angle grain boundaries (>15°) and low-angle grain boundaries (≤15°). Three Ti layers were included for representative statistics. MTEX was used to quantify the proportion of low-angle grain boundaries at different strains (Fig. 9). The results revealed that the relative frequency of the misorientation angle between 2° and 3° was increased from 8.75% to 14.03% and the misorientation angle between 3° and 4° was elevated from 8.00% to 13.01% when the applied strain was increased from 0% to 11.7%. It should be noted that the frequency of misorientation angels (2°−6°) was also significantly enhanced; instead, the tendency of misorientation angles (7°−15°) remained stable. In Fig. 10, we present a close-up view of sub-structural evolution process for clear visualization.

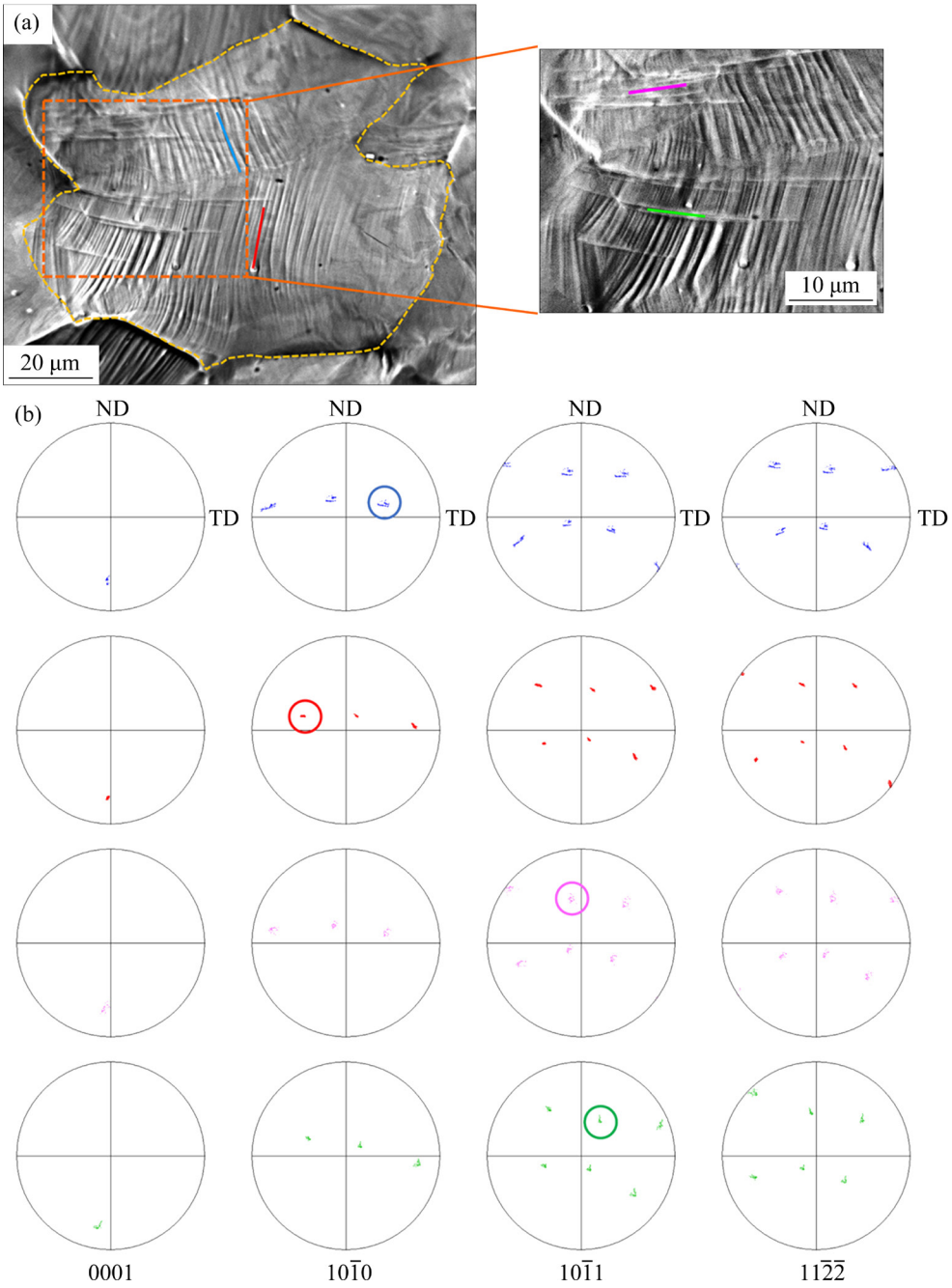

Fig. 7 Quantifying of operative slip system: (a) Slip trace; (b) {0001}, {10$\bar{1}$0}, {10$\bar{1}$1} and {11$\bar{2}\bar{2}$} pole figures

3.3 Quantifying of stress-affected zone

In this section, we attempted to correlate the intragranular deformation inhomogeneity with the interfacial stress-affected zone. The so-called "interface" comprised the Ti/Al interface (interlaminar) and grain boundary (Ti layer or Al layer). The contribution of interlaminar interfaces can be evaluated through the mapping of geometrically necessary dislocations (GNDs). Based on the fact that the quantification of GNDs was closely associated with the dislocation density tensor, there is a lack of curvature tensor along the z direction for two-dimensional EBSD analysis. Therefore, the curvature tensor in the z direction was fitted by the dislocation energy, enabling the direct derivation of GND density from curvature tensor. The working principle and fundamentals for GND calculation can be found in Refs. [12,25]. According to Hull & Bacon model, the energy U of edge and screw dislocations is empirically extrapolated by [26]

$$U_{\text{screw}} = \frac{Gb^2}{4\pi}\ln\frac{R}{r_0} \tag{1}$$

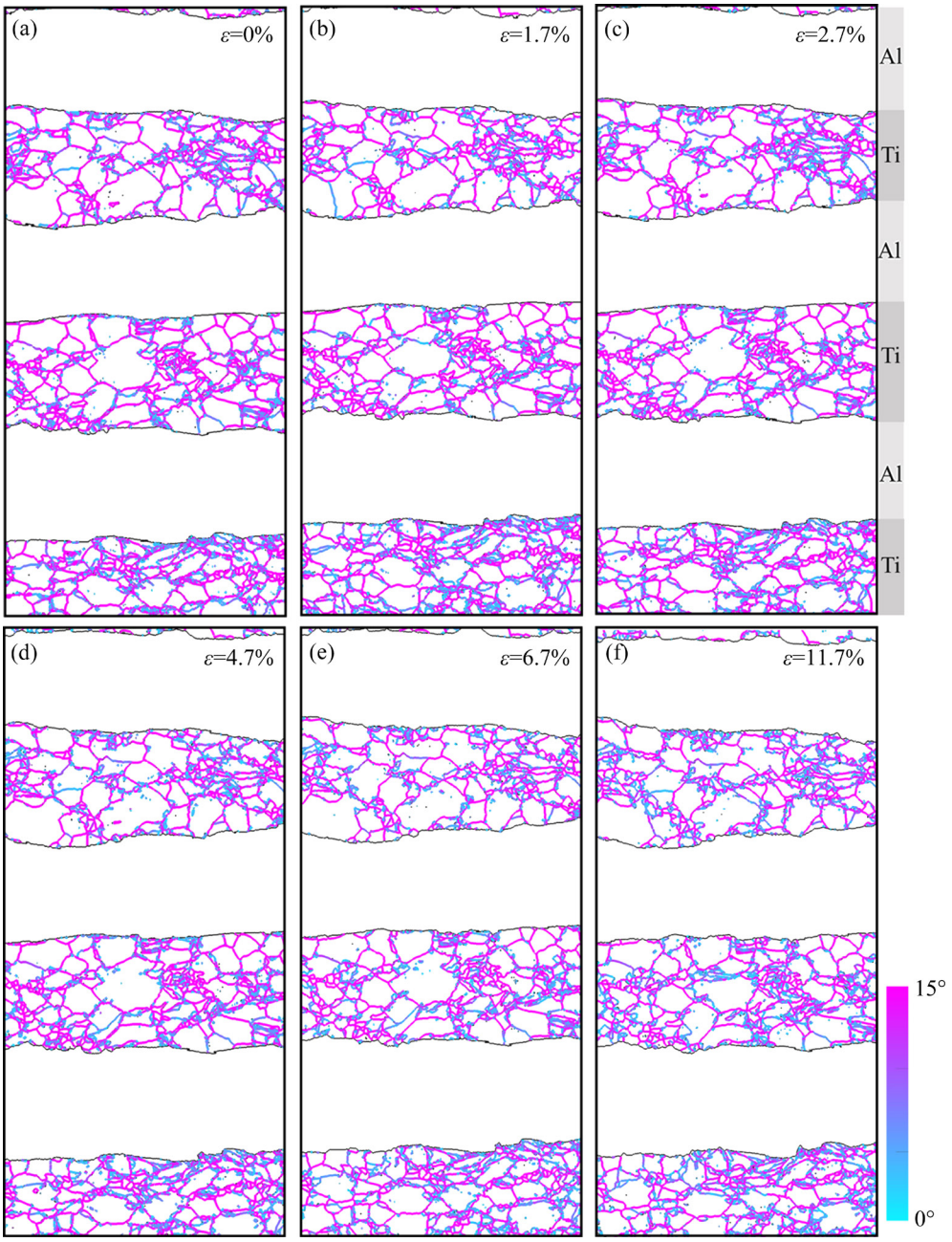

Fig. 8 Distribution of low-angle grain boundaries at different tensile strains: (a) 0%; (b) 1.7%; (c) 2.7%; (d) 4.7%; (e) 6.7%; (f) 11.7%

$$U_{edge}=(1-\nu)U_{screw} \quad (2)$$

where G is the shear modulus; ν is the Poisson's ratio; b is the magnitude of Burgers vector; r_0 is the radius of dislocation center; R is the radius of the maximum action range of stress field of a dislocation. The Al layers, rather than Ti layers, were selected for GND analysis on the basis of the following reasons: (1) The algorithm for calculating GND density in aluminum seemed relatively mature [27−29], and (2) FCC Al was isotropic, and the physics of edge or screw dislocations has been well documented over the past decade [30], in sharp contrast with severely anisotropic hcp Ti.

Figure 11 shows the GND evolution within Al layers during in situ tension. The GND variation in the Al layers was very slight at a low strain level of <2.7%; however, the accumulation of GNDs in the Al layer was clearly observed if the applied strain was further enhanced. A large amount of dislocations seemed to be emitted from the interface, probably due to the deformation incompatibility between Ti and Al constituent layers [31,32], which confirmed the existence of the interfacial stress-

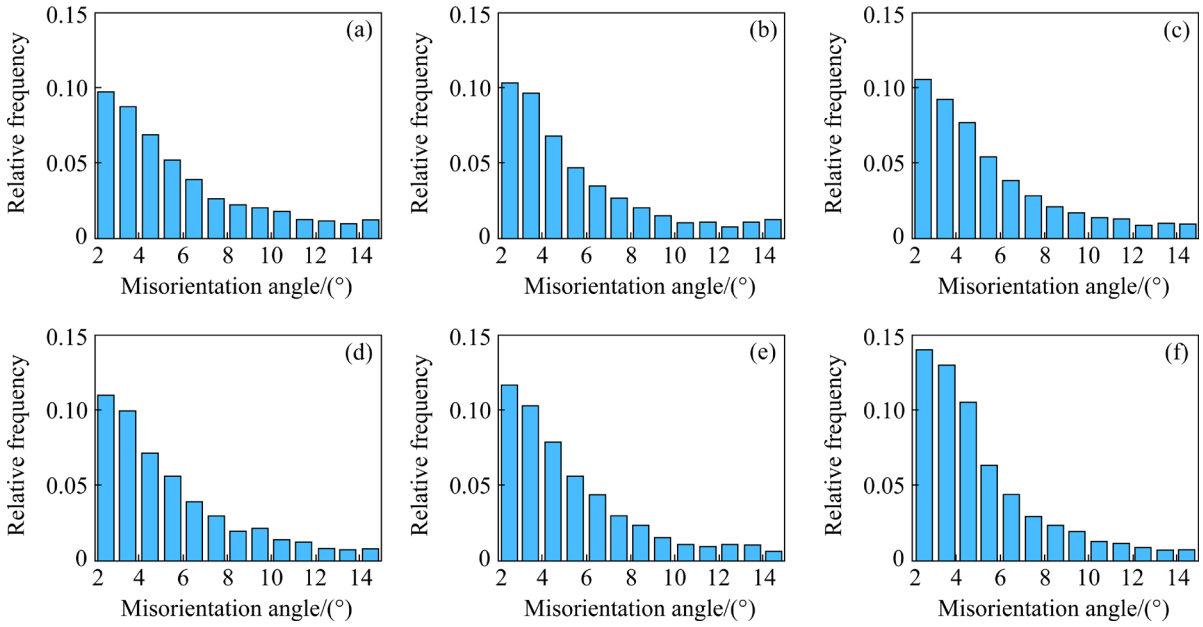

Fig. 9 Distribution histogram of inter-granular misorientation angle in low-angle region at different tensile strains: (a) 0%; (b) 1.7%; (c) 2.7%; (d) 4.7%; (e) 6.7%; (f) 11.7%

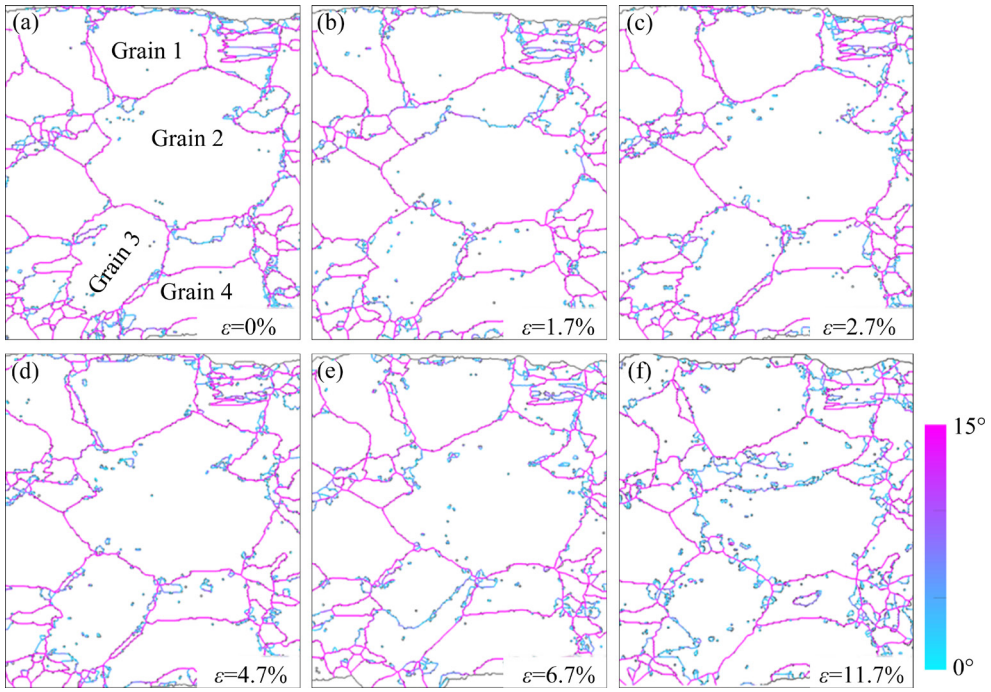

Fig. 10 Close-up view of low-angle grain boundaries within one Ti layer at different tensile strains: (a) 0%; (b) 1.7%; (c) 2.7%; (d) 4.7%; (e) 6.7%; (f) 11.7%

affected zone [33,34]. The accumulation of GNDs at the interfacial stress-affected zone helped with the elevating of strain hardening rate [14], which contributed to the strengthening and excellent ductility. The width of the interfacial stress-affected zone in the present study remained largely constant with a length scale of 20−50 μm. We further verified the distribution of GNDs and the existence of interfacial stress-affected zone by post-mortem SEM characterization. A large amount of slip bands were found near the phase interface (Fig. 12), and their shape and direction were in consistent with the GND distribution (Fig. 11). Additionally, a series of fine cracks were detected, which have not connected with each other to form the main crack. Nevertheless, the presence of many subcritical

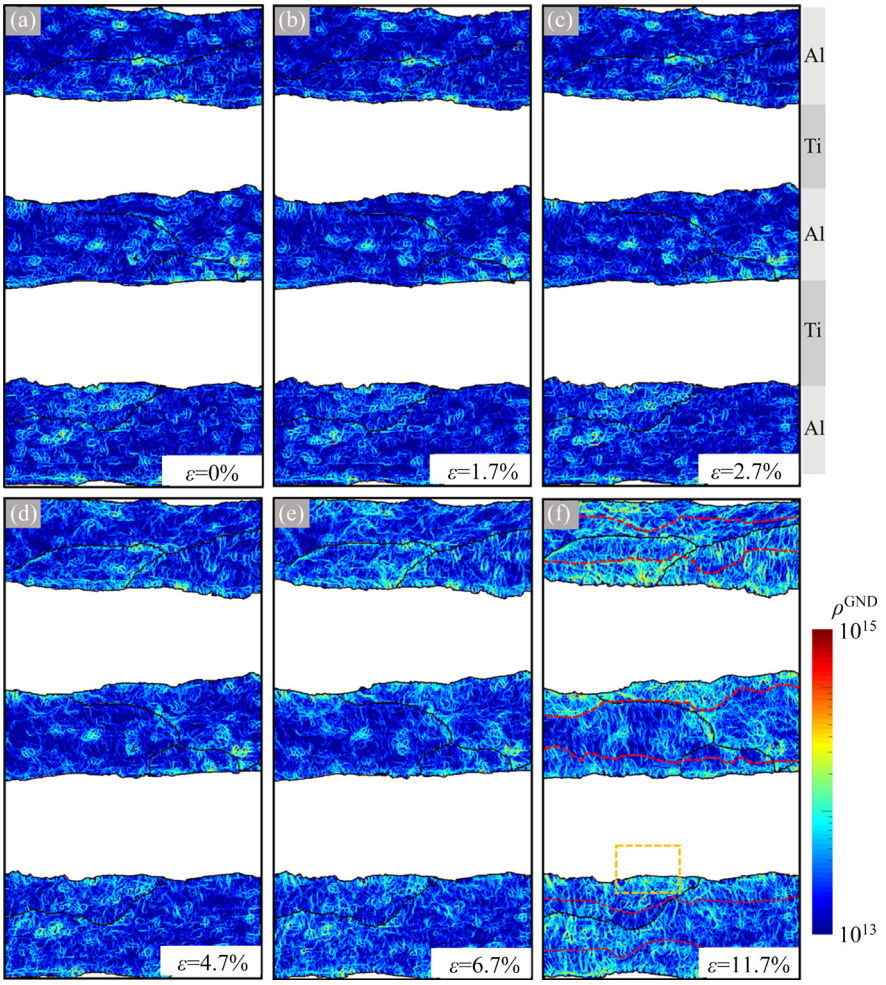

Fig. 11 Spatial distribution and density of GNDs within Al layers at different strains: (a) 0%; (b) 1.7%; (c) 2.7%; (d) 4.7%; (e) 6.7%; (f) 11.7%

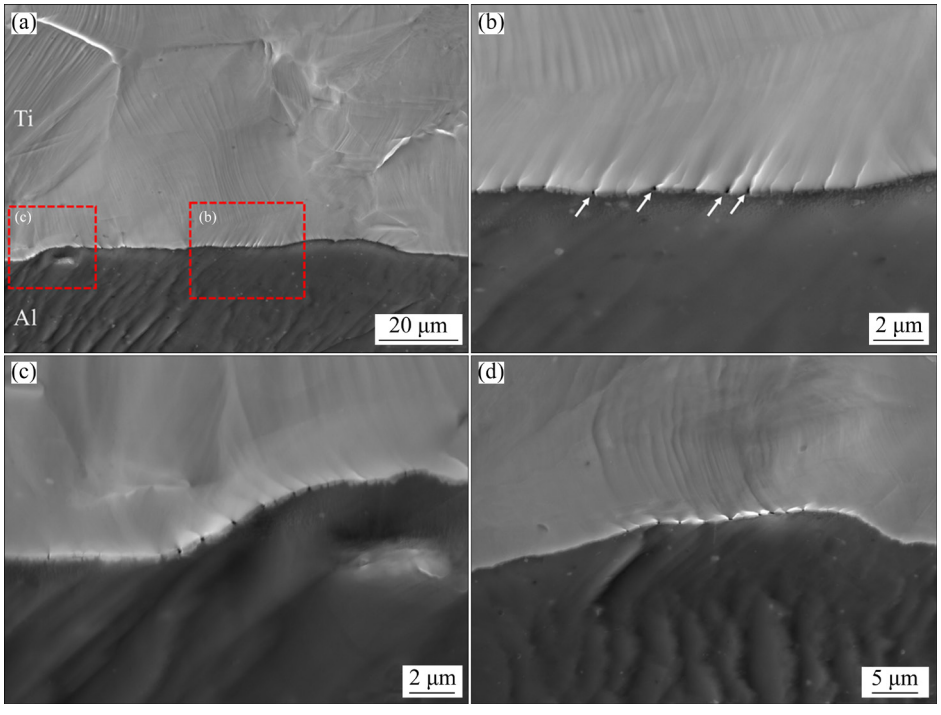

Fig. 12 Post-mortem characterization of localized plastic flow at phase interface between Ti and Al layers

cracks indicated strong interfacial constraint acting onto the crack tip [35,36]. Such a constraint effect was experimentally supported by the GND distribution, peaking at the Ti−Al interface and progressively decreasing when being far away from interface. This rationalizes the intragranular deformation inhomogeneity of Grain 1 and Grain 4, both of which are located at the Ti/Al interface.

Another key factor is the grain boundary, which is thermodynamically unstable, thereby influencing the deformation inhomogeneity within the grain interior [37]. This is because the disordered atomic array at the grain boundary yields a stress field with the stress intensity being progressively degraded when being away from the grain boundary [38]. As an example, reducing the grain size of Mg−Gd alloys suppressed the premature deformation twinning and instead promoted the pyramidal slip, which caused the simultaneous enhancement of strength and ductility [39]. In the present study, it is concluded that the interior of coarse titanium grains may plastically deform more freely, compared to the constituent approaching to the grain boundary; in other words, the grain interior should rotate first with increasing strain, and dislocations accumulated between the rotating part and the unrotated part [40]. The local stress intensity was enhanced with increasing dislocation density, so that the deformation was gradually transferred from the interior to the grain boundary.

It should be highlighted that the grain-level plastic deformation is influenced by the stress field, imparted by both Ti/Al interfaces and grain boundaries [41]. An extreme case is Grain 1 or Grain 4, where the grain approaching to the Ti/Al interface seems difficult to be plastically deformed. The contribution of stress field caused by grain boundaries would be increasingly important when being away from the Ti/Al interface. Therefore, the synergetic constraint of phase interface and grain boundary is believed as the dominated mechanism that accounts for the intragranular deformation inhomogeneity.

4 Conclusions

(1) Multi-layered Ti−Al composites with sharp interlamellar interfaces were prepared by hot rolling of pure Ti and Al foils. In situ EBSD was performed and demonstrated the prismatic $\langle a \rangle$ slip as the crucial deformation mode.

(2) Significant inhomogeneous deformation mode was found within almost all the Ti grains. In particular, the closer to the Ti/Al interface or grain boundary, the less the degree of grain rotation.

(3) The mechanism of the synergetic constraint of the phase interface and grain boundary was proposed to rationalize such an intragranular deformation inhomogeneity.

Acknowledgments

This work was financially supported by the National Natural Science Foundation of China (Nos. 52171117, 52001161, 51927801, 51871111), Jian-Hua Research Foundation of Hebei University of Technology, China (Nos. HB1921, HB1920), and the Natural Science Foundation of Jiangsu Province, China (Nos. BK20200695, BK20202010).

References

[1] LU K. The future of metals [J]. Science, 2010, 328(5976): 319−320.

[2] SHI X H, CAO Z H, FAN Z Y, ECKERT J, QIAO J W. Static coarsening behavior of equiaxed α phase in Ti−8Al−1Mo−1V alloy [J]. Transactions of Nonferrous Metals Society of China, 2021, 31(6): 1628−1640.

[3] XU R R, LI M Q. Quantitative characterization of β-solidifying γ-TiAl alloy with duplex structure [J]. Transactions of Nonferrous Metals Society of China, 2021, 31(7): 1993−2004.

[4] WILLIAMS J C, BLACKBURN M J. The identification of a non-basal slip vector in titanium and titanium−aluminum alloys [J]. Physica Status Solidi (b), 1968, 25(1): K1−K3.

[5] XU S, GONG M Y, JIANG Y Y, SCHUMAN C, LECOMTE J S, WANG J. Secondary twin variant selection in four types of double twins in titanium [J]. Acta Materialia, 2018, 152: 58−76.

[6] LI H, MASON D E, BIELER T R, BOEHLERT C J, CRIMP M A. Methodology for estimating the critical resolved shear stress ratios of α-phase Ti using EBSD-based trace analysis [J]. Acta Materialia, 2013, 61: 7555−7567.

[7] LIU N, WANG Y, HE W J, LI J, CHAPUIS A, LUAN B F, LIU Q. Microstructure and textural evolution during cold rolling and annealing of commercially pure titanium sheet [J]. Transactions of Nonferrous Metals Society of China, 2018, 28(6): 1123−1131.

[8] FAN R L, WU Y, CHEN M H, XIE L S. Relationship among microstructure, mechanical properties and texture of TA32 titanium alloy sheets during hot tensile deformation [J]. Transactions of Nonferrous Metals Society of China, 2020, 30(4): 928−943.

[9] VAJPAI S K, OTA M, ZHANG Z, AMEYAMA K. Three-dimensionally gradient harmonic structure design: An

integrated approach for high performance structural materials [J]. Materials Research Letters, 2016, 4(4): 191−197.

[10] GAO H, HUANG Y. Geometrically necessary dislocation and size-dependent plasticity [J]. Scripta Materialia, 2003, 48: 113−118.

[11] NIX W D, GAO H. Indentation size effects in crystalline materials: A law for strain gradient plasticity [J]. Journal of the Mechanics and Physics of Solids, 1998, 46(3): 411−425.

[12] ASHBY M F. The deformation of plastically non-homogeneous materials [J]. Philosophical Magazine, 2006, 21(170): 399−424.

[13] LU K. Nanomaterials: Making strong nanomaterials ductile with gradients [J]. Science, 2014, 345(6203): 1455−1456.

[14] MA X L, HUANG C X, MOERING J, RUPPERT M, HÖPPEL H W, GÖKEN M, NARAYAN J, ZHU Y T. Mechanical properties of copper/bronze laminates: Role of interfaces [J]. Acta Materialia, 2016, 116: 43−52.

[15] YANG D K, CIZEK P, FABIJANIC D, WANG J T, HODGSON P D. Work hardening in ultrafine-grained titanium: Multilayering and grading [J]. Acta Materialia, 2013, 61: 2840−2852.

[16] LI J, CHEN S, WU X, SOH A K. A physical model revealing strong strain hardening in nano-grained metals induced by grain size gradient structure [J]. Materials Science and Engineering A, 2015, 620: 16−21.

[17] WU H, FAN G H. An overview of tailoring strain delocalization for strength-ductility synergy [J]. Progress in Materials Science, 2020, 113: 100675.

[18] HUANG M, XU C, FAN G H, MAAWAD E, GAN W M, GENG L, LIN F X, TANG G Z, WU H, DU Y, LI D Y, MIAO K S, ZHANG T T, YANG X S, XIA Y P, CAO G J, KANG H J, WANG T M, XIAO T Q, XIE H L. Role of layered structure in ductility improvement of layered Ti−Al metal composite [J]. Acta Materialia, 2018, 153: 235−249.

[19] WU X L, YANG M X, YUAN F P, WU G, WEI Y, HUANG X, ZHU Y. Heterogeneous lamella structure unites ultrafine-grain strength with coarse-grain ductility [J]. Proceedings of the National Academy of Sciences, 2015, 112(47): 14501−14505.

[20] LI D, WANG B, LUO L, LI X, XU Y, LI B, HAWEZY D, WANG L, SU Y, GUO J, FU H. Effect of processing parameters on the microstructure and mechanical properties of TiAl/Ti_2AlNb laminated composites [J]. Journal of Materials Science & Technology, 2022, 109: 228−244.

[21] WU H, FAN G, HUANG M, GENG L, CUI X, XIE H. Deformation behavior of brittle/ductile multilayered composites under interface constraint effect [J]. International Journal of Plasticity, 2017, 89: 96−109.

[22] LI D Y, FAN G H, HUANG X X, JUUL JENSEN D, MIAO K S, XU C, GENG L, ZHANG Y B, YU T B. Enhanced strength in pure Ti via design of alternating coarse- and fine-grain layers [J]. Acta Materialia, 2021, 206: 116627.

[23] ZHANG M, LUAN B F, CHU L H, GAO B, WANG L, YUAN G H, LIU Q. Deformation kinking in β-treated zirconium impacted by split Hopkinson pressure bar [J]. Scripta Materialia, 2020, 187: 379−383.

[24] CHUN Y B, BATTAINI M, DAVIES C H J, HWANG S K. Distribution characteristics of in-grain misorientation axes in cold-rolled commercially pure titanium and their correlation with active slip modes [J]. Metallurgical and Materials Transactions A, 2010, 41(13): 3473−3487.

[25] NYE J F. Some geometrical relations in dislocated crystals [J]. Acta Metallurgica, 1953, 1: 153−162.

[26] HULL D, BACON D J. Introduction to dislocations [M]. Butterworth−Heinemann, 2001.

[27] ZHANG C L, GODFREY A, ZHANG Y, WU G L, XU R, LIU W, JUUL JENSEN D. Dislocation density in fine grain-size spark-plasma sintered aluminum measured using high brightness synchrotron radiation [J]. Materials Letters, 2020, 269: 127653.

[28] WANG Q, HE X, DENG Y L, ZHAO J H, GUO X B. Experimental study of grain structures evolution and constitutive model of isothermal deformed 2A14 aluminum alloy [J]. Journal of Materials Research and Technology, 2021, 12: 2348−2367.

[29] ZHANG S Q, LIU W, WAN J F, MISRA R D K, WANG Q, WANG C. The grain size and orientation dependence of geometrically necessary dislocations in polycrystalline aluminum during monotonic deformation: Relationship to mechanical behavior [J]. Materials Science and Engineering A, 2020, 775: 138939.

[30] CHENG W J, LIU W, FAN X B, YUAN S J. Cooperative enhancements in ductility and strain hardening of a solution-treated Al−Cu−Mn alloy at cryogenic temperatures [J]. Materials Science and Engineering A, 2020, 790: 139707.

[31] YANG M X, PAN Y, YUAN F P, ZHU Y T, WU X L. Back stress strengthening and strain hardening in gradient structure [J]. Materials Research Letters, 2016, 4(3): 145−151.

[32] WU X L, ZHU Y T. Heterogeneous materials: A new class of materials with unprecedented mechanical properties [J]. Materials Research Letters, 2017, 5(8): 527−532.

[33] HUANG C X, WANG Y F, MA X L, YIN S, HÖPPEL H W, GÖKEN M, WU X L, GAO H J, ZHU Y T. Interface affected zone for optimal strength and ductility in heterogeneous laminate [J]. Materials Today, 2018, 21(7): 713−719.

[34] ZHOU Y, HE W J, MA J T, CHEN Z J, LIU Q. Annealing hardening and deformation behavior of layered gradient Zr−Ti composite [J]. Transactions of Nonferrous Metals Society of China, 2021, 31(8): 2358−2371.

[35] WU H, HUANG M, LI Q G, WU J Y, LI J K, WANG Z, FAN G H. Manipulating the plastic strain delocalization through ultra-thinned hierarchical design for strength−ductility synergy [J]. Scripta Materialia, 2019, 172: 165−170.

[36] WANG Y F, WANG M S, YIN K, HUANG A H, LI Y S, HUANG C X. Yielding and fracture behaviors of coarse-grain/ultrafine-grain heterogeneous-structured copper with transitional interface [J]. Transactions of Nonferrous Metals Society of China, 2019, 29(3): 588−594.

[37] LU K. Stabilizing nanostructures in metals using grain and twin boundary architectures [J]. Nature Reviews Materials, 2016, 1(5): 16019.

[38] KUHR B, FARKAS D, ROBERTSON I M, JOHNSON D, WAS G. Stress localization resulting from grain boundary dislocation interactions in relaxed and defective grain boundaries [J]. Metallurgical and Materials Transactions A, 2019, 51(2): 667−683.

[39] LUO X, FENG Z Q, YU T B, LUO J Q, HUANG T L, WU G L, HANSEN N, HUANG X X. Transitions in mechanical behavior and in deformation mechanisms enhance the strength and ductility of Mg−3Gd [J]. Acta Materialia, 2020, 183: 398−407.
[40] WU X L, ZHU Y T, LU K. Ductility and strain hardening in gradient and lamellar structured materials [J]. Scripta Materialia, 2020, 186: 321−325.
[41] WU H, HUANG M, LI X W, XIA Y P, WANG Z, FAN G H. Temperature-dependent reversed fracture behavior of multilayered TiB_w/Ti−Ti(Al) composites [J]. International Journal of Plasticity, 2021, 141: 102998.

层状 Ti−Al 复合材料界面约束导致的晶内变形不均匀性

倪新波[1]，刘壮壮[1]，缪克松[2,3]，冷金凤[1]，范国华[2]，滕新营[1]，吴 昊[2]

1. 济南大学 材料科学与工程学院，济南 250022；
2. 南京工业大学 先进轻质高性能材料研究中心，南京 211816；
3. 哈尔滨工业大学 材料科学与工程学院，哈尔滨 150001

摘 要：以纯钛箔和纯铝箔为原料，通过热压和热轧制制备层状 Ti−Al 复合材料。使用原位电子背散射衍射技术，研究层状复合材料拉伸过程中的取向演化和形变微结构特征。结果表明，Ti 晶粒内部塑性变形存在不均匀性，即越靠近晶界或 Ti/Al 层状界面，Ti 晶粒的塑性变形越困难。这种晶内变形不均匀性主要来自于晶界和 Ti/Al 相界的协同约束效应。因此，本研究提供了一种通过充分利用界面约束效应来调控塑性变形行为从而实现性能优化的新策略。

关键词：层状复合材料；塑性变形；电子背散射衍射；界面约束

(Edited by Bing YANG)